Cytoskeletal Proteins at the Lipid Membrane

Wolfgang H. Goldmann[1,2,*], Burkhard Bechinger[3], *and* Tanmay Lele[4]

Contents

Abstract

The interface at the cell membrane and cytosol offers a wealth of possibilities for intermolecular interactions. Molecular anchors, -bridges, -transmembrane connectors as well as cascades of proteins inside the cell regulate the bidirectional exchange of

* Corresponding author. Tel: +49 (0)9131-85-25605; Fax: +49 (0)9131-85-25601
E-mail address: wgoldmann@biomed.uni-erlangen.de (W.H. Goldmann).

[1] Massachusetts General Hospital, Harvard Medical School, Charlestown, MA 02129, USA
[2] Center for Medical Physics and Technology, Biophysics Group, Friedrich-Alexander-University of Erlangen-Nuremberg, Henkestrasse 91, 91052 Erlangen, Germany
[3] Université Louis Pasteur Strasbourg, CNRS, Institut de Chimie, UMR 7177-LC3, 4, rue Blaise Pascal, 67070 Strasbourg, France
[4] Department of Chemical Engineering, University of Florida, Museum Road, Bldg. 723, Gainesville, FL 32611, USA

information between the cell and extracellular environment. Previously, little attention has been given to lipids that are essential for the membrane architecture and for the regulation and function of membrane-associated cytoskeletal proteins. The emergence of new biophysical techniques has spurred rapid acceleration in the ability of researchers to investigate and understand protein–lipid membrane interactions in artificial systems as well as in cells. Stopped-flow kinetics, differential scanning calorimetry (DSC), solid-state nuclear magnetic resonance (NMR) spectroscopy as well as fluorescence recovery after photobleaching (FRAP) will be described and their application will be discussed.

1. INTRODUCTION

Proteins that interface between the cytoskeleton and the plasma membrane control cell shape and tension, and stabilize attachments to other cells and to extracellular substrates. Signals that reach the cell surface and induce intracellular responses may be hormonal, chemical or mechanical. Similarly, signals from inside the cell can give rise to changes in cell membrane architecture, whilst signals, transmitted laterally, within the plane of the lipid membrane may have long-range effects on the cell surface [1–6].

Many proteins exist in soluble forms in the cytoplasm and fractions may associate transiently with the boundary of the lipid membrane. In an aggregate form, proteins (and their complexes) are likely to interact in a two-step mechanism: an initial electrostatic attraction is followed by some form of lipid insertion, which may be associated with protein refolding events. Conformational changes only occur when the lipid membrane finds compatible and complementary configurations such as exposed combinations like α-helices or β-strands on the protein. The assumption is that surface binding to polar lipid head groups is achieved by exposing amphipathic secondary structures, predominantly α-helices. Insertion into one-half of the hydrophobic bilayer requires β-barrels or hydrophobic α-helices. Even when only the amino acid sequence is known, the predictive methods to describe these lipid-binding structures are often accurate. A hydrophobicity index based on physio-chemical properties for each amino acid and the probability, that a protein is membrane spanning or inserting, is derived by hydrophobic plots. We used purpose-written computer matrices to discriminate between liquid surface-seeking and transmembrane configurations of α-helices [7]. By applying this method, we are able to predict potential lipid-binding motifs for several proteins with high accuracy including Cap-Z, filamin, α-actinin, PR3 and other membrane-associated proteins [7–11].

Since new physical techniques have become available, investigating the lipid membrane interface has gained more interest among biochemists and cell biologists. In this chapter, we describe in Section 2 the stopped–flow, in Section 3 differential scanning calorimetric (DSC) and in Section 4 solid–state nuclear magnetic resonance (NMR) measurements to study interactions between proteins and lipid membranes. We further summarize in Section 5 fluorescence recovery after

photobleaching (FRAP) studies aimed at elucidating events accompanying protein binding in cells.

2. STOPPED-FLOW SPECTROPHOTOMETER

The principle of this method is to mix two reactant solutions by rapid flow, to stop the flow and to observe the change continuously in an observation cell. The application and limitations are discussed in detail by Gutfreund [12], Bernasconi [13] and Goldmann *et al.* [14].

All experiments that are described here were carried out on an SF 61 stopped-flow spectrophotometer supplied by Hi-Tech-Scientific, Salisbury, UK. A schematic representation of the unit is shown in Fig. 1. The unit consists of two 1 ml Hamilton drive syringes, which can be filled from reservoirs. Syringes are driven simultaneously by compressed air from a pressure-driven ram mounted upon the base unit. At 3 bar normal operating pressure, the dead time is measured to be around 1.5 ms. Solutions are rapidly mixed in a quartz observation/reaction cell that can be controlled thermostatically. The cell is set in light scatter mode with 10 nm path length. Light is transmitted to the cell *via* a quartz fiber optic light guide. Emitted light from the reaction/observation cell is sent *via* a silvered quartz rod to the photomultiplier. The flow is stopped using another 1 ml Hamilton syringe. A micro-switch is pressed by the stopping syringe to give a trigger pulse. The temperature is indicated by a thermocouple placed in the fluid-handling unit and maintained by an external heating device.

A purpose-built stabilized power supply is the energy source for the 100 W high-pressure mercury or Xenon lamp. Light is monochromated with a band pass width of 5 nm by a M300 monochromator. Light scatter measurements of protein–protein and/or protein–lipid interactions are followed at 355 nm and light is passed through a Schott UG11 filter to cut higher order deflections. Emitted light is
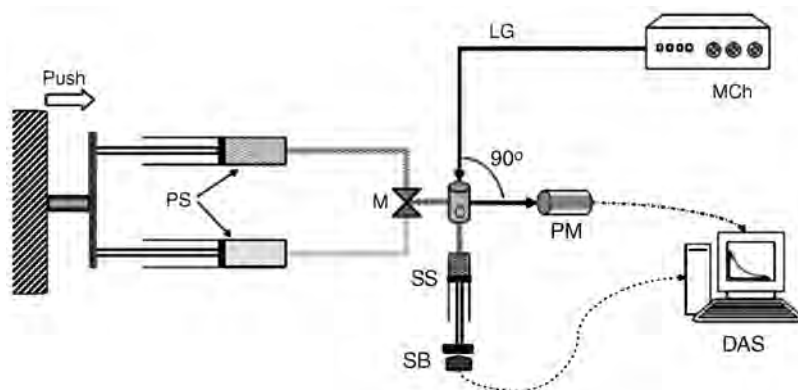

Figure 1 Schematic representation of the stopped–flow apparatus. PS, Probe syringe; M, Mixer; C, Reaction/observation cell; SS, Stopping syringe; SB, Stopping block/micro-switch; PM, Photomultiplier; LG, Light guide; MCh, Monochromator; DAS, Data acquisition system.

detected at 90° for light scatter measurements through a Schott KV 393 filter. The signal is electronically filtered by an unit gain amplifier. The time constant is normally 5% of the half time of an observed protein–protein reaction. High-tension power to drive the photomultiplier is adjusted so that the output is between -1.0 V and -5.0 V depending on the reaction. The signal is then offset to zero voltage, using the backing off on the unity gain amplifier. Transient recorders are triggered by a 5.0 V pulse opening the micro-switch on the stopping block of the stopped-flow machine. The analogue signal from the photomultiplier is then digitized before being transferred to a computer for further analysis. The data are analyzed either as single or averaged traces.

2.1. 'Slow' Temperature Jump Apparatus

Stopped-flow for a temperature jump has been modified according to Goldmann and Geeves [15] (Fig. 2). This method is capable of measuring temperature differences larger than 10°C in less than 150 ms and is sensitive and reliable for measuring myosin II–lipid insertion events.

In this example, a myosin II—lipid solution is held in a single syringe 15°C (T_1). A driving mechanism operated by compressed air pushes the sample into the observation cell. The tubing and the cell are immersed at 30°C (T_2). Temperature regulation is provided by an external heater and an internal thermocouple. A micro-switch is triggered by a front stop that initiates signal detection. The system is designed to allow the solution to equilibrate to the new temperature (T_2)

Figure 2 Water circulation at the stopped-flow apparatus. From left to right: electronics unit; sample-handling unit; ice container for cooling and hot plate for heating the circulating solution.

in the cell. Changes in light scatter signal at 355 nm and at a 90° angle are recorded with time. The optical and detection systems are discussed in the stopped-flow spectrophotometer chapter.

2.2. Results

Using the modified stopped-flow apparatus we can show that light scattering can be applied to measure the affinity of myosin II to lipid vesicles. This method is a development for experimental work by Goldmann *et al.* [16] and the analysis by Michel *et al.* [17]. In brief, a solution of 120 μl myosin II–lipid is prepared and prior to experimentation is exposed to 10 cycles of 'freeze-thaw', i.e., cooling of samples to 5°C and warming to 37°C. Then it is filled into the reservoir syringe of the stopped-flow (kept at 10°C) and injected into the reaction/observation chamber (kept at 37°C). Over time, as the solution warms, the light scatter signal (355 nm) is followed at the phase transition (T_M, *melting*) point of dimyristoylphosphatidylcholine (DMPC) and dimyristoylphosphatidylglycerol (DMPG) lipids and molar ratio of 50:50.

As shown in Fig. 3, the light scatter signal for pure lipids is the largest and with increasing myosin II concentrations ($0.25 \rightarrow 3.50$ μM) the signal decreases. Based on the relationship

$$\ln(I - I_0/I_0) = A - KxC \tag{1}$$

where, I_0 is the scatter signal before and I after the phase transition, A the intercept of the y-axis, K (association constant) the molar affinity of myosin II to lipids and C the concentration of myosin II. Since the values of I and I_0 are not very accurate, the Boltzmann-Regression curve was used,

$$y = \frac{A_1 - A_2}{1 e^{(x-x_0)/\Delta x} + A_2} \tag{2}$$

where, A_1 and A_2 are I and I_0, respectively, and x_0 the center of the distribution, Δx the width of the slope at point x_0. Plotting the curves in Fig. 3 using the linear
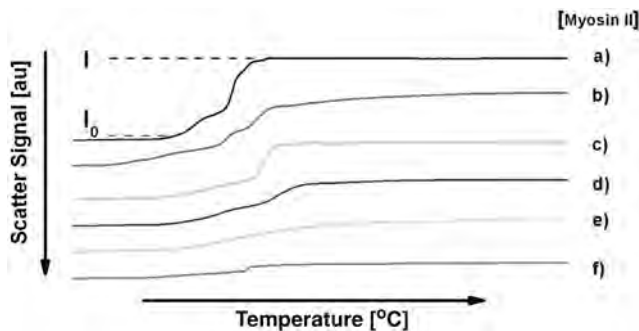

Figure 3 Light scatter signals. Temperature-induced light scatter changes between 20°C and 25°C at 355 nm. Conditions: Lipid and myosin II concentrations: 1.82 mM and (a) 0 μM, (b) 0.25 μM, (c) 0.5 μM, (d) 1.5 μM, (e) 2.5 μM and (f) 3.5 μM, respectively.

relationship, a molar affinity was determined for myosin II to lipid vesicles of K (association constant) $= 0.59 \times 10^6\,\text{M}^{-1}$. The affinity of protein association/insertion into lipid membranes is comparable to other membrane-associated proteins like talin ($K = 2.9 \times 10^6\,\text{M}^{-1}$) and vinculin ($K = 0.33 \times 10^6\,\text{M}^{-1}$) [16]. For a control bovine serum albumin (BSA) was used.

2.3. Binding Affinity of Myosin II (Associated/Inserted-Lipid) to Actin

The binding affinity of actin to myosin II (bound to lipid vesicles) at a constant temperature using the stopped-flow method was assayed and compared to myosin II and actin. Fig. 4 is a typical trace of myosin II binding to actin. A double exponential fit shows a rate of association for $k_{+1} = 3.86\,\text{s}^{-1}$ and for $k_{+2} = 0.72\,\text{s}^{-1}$ at $1\,\mu\text{M}$ actin and $5\,\mu\text{M}$ myosin II concentration at 355 nm. The binding kinetics measured for actin and myosin II bound to lipids also showed a similar value. Unfortunately, the noise level between 0 and 0.2 s was higher and difficult to fit. To circumvent this problem, the method of 'stationary titration' was employed using the stopped-flow apparatus. The light scatter signal at 355 nm was measured using actin concentrations between $0.25 \rightarrow 4\,\mu\text{M}$ and at constant myosin II concentration ($5\,\mu\text{M}$) in the presence/absence of lipids after 1 s of injection into the reaction/observation chamber at 4 bar. The data were analyzed according to Hiromi [18], using the following equation:

$$[A]_0/\alpha = \big([M]_0 + K_\text{d}\big) + ([A]_0 - \alpha[M]_0) \tag{3}$$

where $[A]_0 = $ actin and $[M]_0 = $ myosin II concentration at $t = 0$ s; $K_\text{d} = $ binding (dissociation) constant ($K_\text{d} = 1/K$), and $\alpha = $ the fractional saturation of myosin II
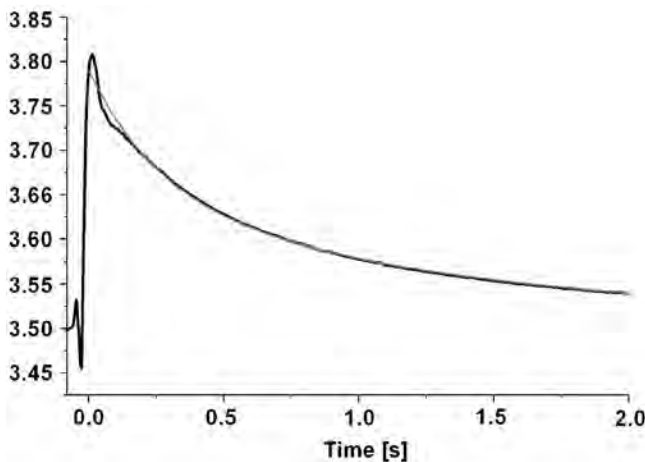

Figure 4   Stopped-flow experiments. Averaged stopped-flow traces of myosin II binding to actin ($n = 3$) with a super-imposed double exponential fit. Rates of association, $k_{+1} = 3.86\,\text{s}^{-1}$ and $k_{+2} = 0.72\,\text{s}^{-1}$. Conditions: actin $= 1\,\mu\text{M}$, myosin II $= 5\,\mu\text{M}$, light scatter signal at 355 nm, and temperature $= 23\,^\circ\text{C}$.
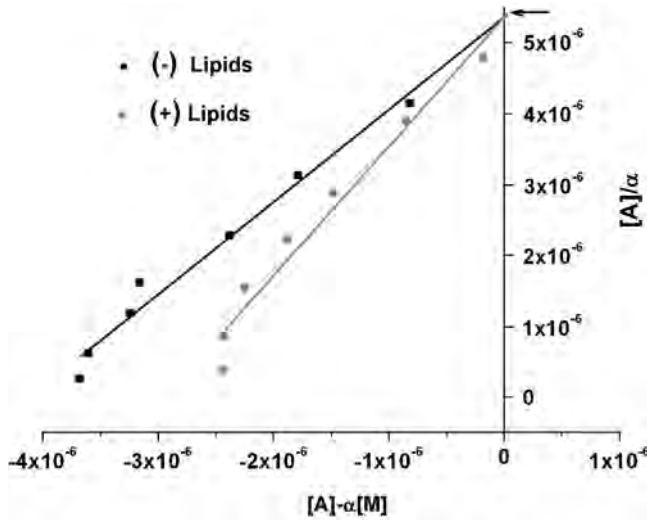
Figure 5 Binding kinetics. A plot of $[A]-\alpha[M]$ as a function of $[A]/\alpha$. The linear fit shows an intercept with the y-axis that equals ($[M]_0+K_d$). K_d for myosin II (bound to lipids) and actin = 0.362 μM; K_d for myosin II and actin = 0.357 μM.

by actin. α is defined by the relationship,

$$\alpha = \frac{I_0 - I}{I_0 - I_\infty} \tag{4}$$

where, I_0 = light scatter signal in the absence and I_∞ = at infinitely high-actin concentration. Using these results, $[A]-\alpha[M]$ (x-axis) was plotted against $[A]/\alpha$ (y-axis) to give a linear relationship where, the intercept is the dissociation constant, K_d.

Results from measurements using equation (3) show a K_d for actin−myosin II of 0.357 μM and actin−(myosin II bound to lipid) of 0.362 μM, respectively (Fig. 5). The results are comparable with other membrane-associated proteins [16]. Figure 6 is a schematic representation of actin−myosin II and actin–myosin II−lipid binding.

3. DIFFERENTIAL SCANNING CALORIMETRY (DSC)

DSC is the most direct experimental technique to resolve the energy of conformational transitions of biological macromolecules. It provides an immediate access to the thermodynamic mechanism that governs a conformational equilibrium, i.e., between folded and unfolded forms of a protein by measuring the temperature dependence of partial heat capacity, ΔC_p, a basic thermodynamic property. The theory of DSC and the thermodynamic interpretation of the experiment have been the subject of excellent reviews [19–21]. Here, a basic description of the principle of the DSC method will be provided with special
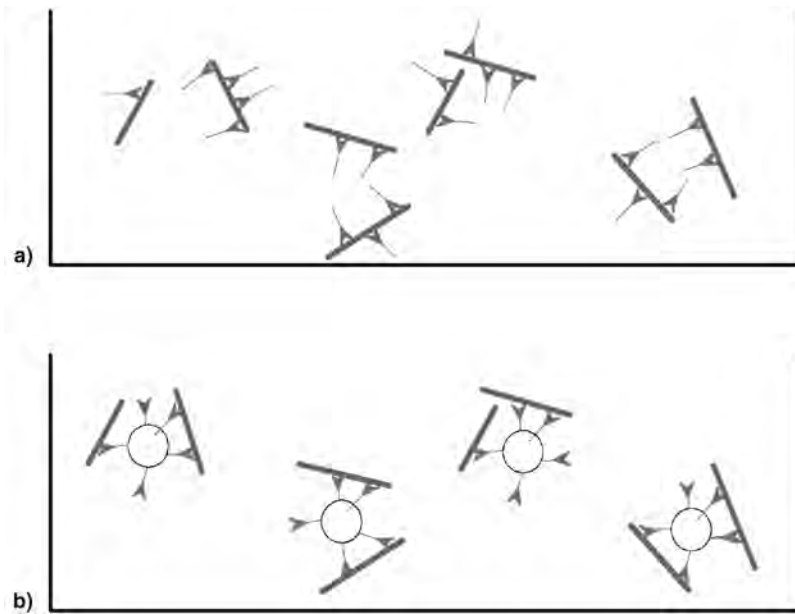
Figure 6 Schematic representation of protein–lipid interaction. Schematic view of (a) myosin II (green) and putative binding to actin (red) and (b) myosin II (bound to lipid vesicles) and actin (please see plate no. 5 in the color section).

emphasis on the potential of DSC to analyze the energetics of protein–lipid association/insertion reactions.

Phospholipids can exist in solvent in a 'gel-like' (*ordered*) as well as 'fluid-like' (*disordered*) phase. The change from a gel to fluid-like phase of a solvated membrane is called its phase transition or (*melting point*). As shown in Fig. 7, this change in specific heat profile has a calorimetric maximum. Before reaching the main phase transition temperature (T_M), some lipids show a pre-transition phase (T_V) at which the 'gel-like' membrane changes from a lamellar ($L_{\beta'}$) to a ripple ($P_{\beta'}$) phase and then proceeds into the fluid phase (L_α).

The saturated covalent bonds in the alkyl chains of lipids can assume many torsion angles. The flexibility of these covalent bonds provides many degrees of freedom. High-energy conformations reduce significantly the *all-trans* configurations and allow any angle of rotation. The phase change from ordered to disordered behavior (*melting*) is regarded as first-order phase transition that follows Gibb's law:

$$\Delta G = \Delta H - T_M \Delta S = 0; \quad \text{or} \quad T_M = \Delta H / \Delta S. \tag{5}$$

where, ΔS = entropy, ΔH = enthalpy and ΔG = free (Gibb's) energy. Using an experimentally determined heat capacity (C_p), it allows the determination of the phase change enthalpy,

$$\Delta H = \int_{gel}^{fluid} C_p \Delta T; \quad \Delta S = \Delta H / T_M. \tag{6}$$
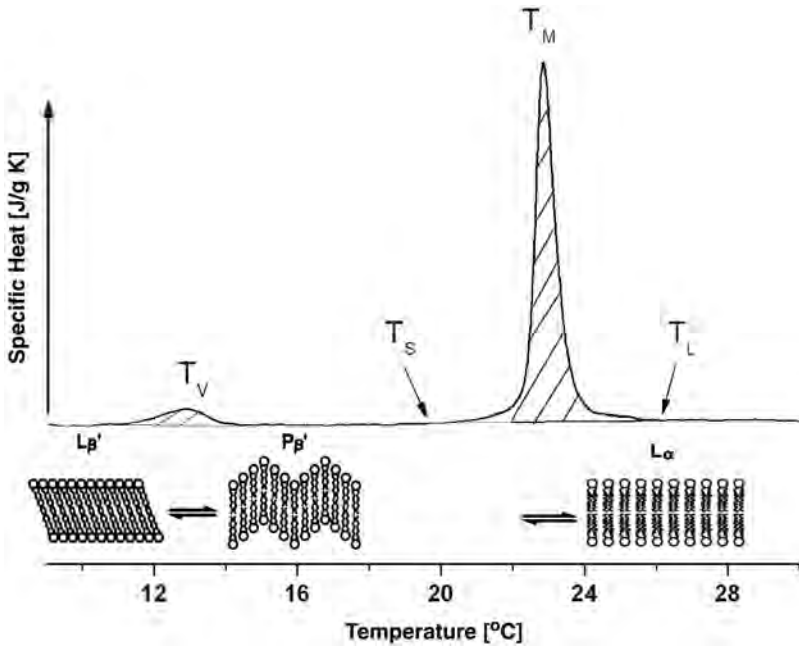
Figure 7 Differential scanning calorimetry. Heat capacity curves and thermotropic phase transitions of DMPC/DMPG vesicles.

From a kinetic view, the melting point is the state where the gel and fluid phase are in equilibrium,

$$K \equiv 1 = \frac{P_{\text{fluid}}(T_M)}{P_{\text{gel}}(T_M)}. \tag{7}$$

The equilibrium constant, K is determined by the relationship,

$$K = e^{-\Delta G/RT} = e^{-(\Delta H - T\Delta S)/RT} \tag{8}$$

where $K = 1$ at $\Delta G = 0$. Since the heat capacity is at a maximum at the phase transition (*melting*) point, the enthalpy fluctuation is therefore also at a maximum. Enthalpy also fluctuates with the surface area, i.e., 'fluid-like' lipids $>$ 'gel-like' lipids and the size, i.e., the volume of lipid molecules is assumed to be constant. The principle of the DSC apparatus is shown in Fig. 8.

The heating of the sample and reference solution is performed at a preset heating rate, $\beta = \Delta T/\Delta t$, where the temperature of the system is determined by $T = T_0 + \beta xt$; (T_0 is the temperature at $t = 0$). The principle of DSC requires the temperature of the sample (probe, T_P) and reference (T_R) solution to remain constant, i.e., $T = T_P = T_R$. At an endothermic phase transition of the sample solution, this has to be heated to a higher degree compared to the sample solution to keep both temperatures at the same level. The heat output for the sample (P_P) will be larger than for the reference (P_R), therefore the difference of the heat
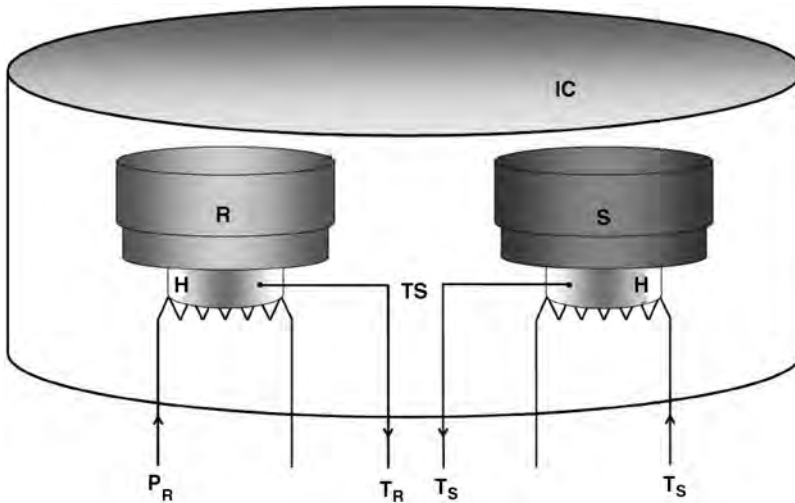
Figure 8   Schematic representation of the DSC apparatus. S, sample cell; R, reference cell; H, heating coil; IC, insulating casing; TS, temperature sensor; T_S and T_R are the currently measured temperatures in sample- and reference cell and (P_R; left) and ($T_S = P_S$; right) are the heat output for the reference and sample cell.

output, ΔP equals P_P–P_R. This is reflected in the heat capacities $\Delta C(T)$ between sample and reference which is proportional to

$$\Delta C(T) = C_p - C_R = \Delta P(T)/\beta. \tag{9}$$

In DSC thermograms, the difference of heat output ΔP is plotted against the temperature T. At the known heat rate, β the heat capacity difference $\Delta C(T)$ between the sample and reference solution as well as the partial dissipation of energy in molar heat capacity can be determined. Figure 7 shows an example of a thermogram for a DMPC and DMPG vesicle solution: pre-transition (T_V) at 13°C and main transition (T_M) at 23°C. Integrating between the start (T_S) and endpoint (T_L) of the DSC temperature signals determine the change in enthalpy

$$\int_{T_L}^{T_S} C_U \Delta T = \Delta_U H \tag{10}$$

A differential scanning calorimeter Q100 from TA Instruments (Fig. 9) was used and the reservoirs for the sample and reference solution are made of stainless steel and to hold a volume of $\sim$100 μl each. Lipid–buffer solutions were placed in the reference cell and the lipid-myosin-II-buffer solutions in the sample cell. Under sealed conditions, both solutions were heated/cooled at a rate, β at 0.5°C/min between +7°C and +35°C in six cycles until the equilibrium of the phase transition enthalpy was reached, using a mixture of DMPC and DMPG at a molar ratio 50:50. A phase transition was observed at $\sim$23°C. Data analysis was performed using the software from *Universal Analysis 2000* (TA Instruments) and *Origin 7G*.
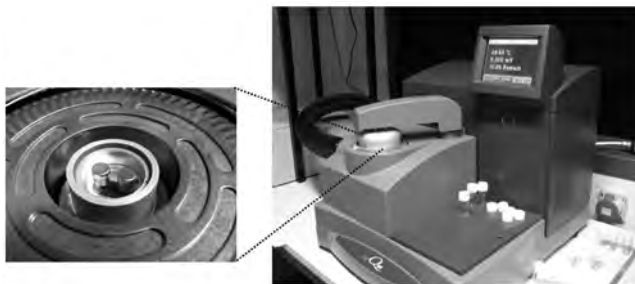
Figure 9 The calorimeter. Image of a calorimeter from TA Instruments (right) and sample and reference cell (arrows, left).
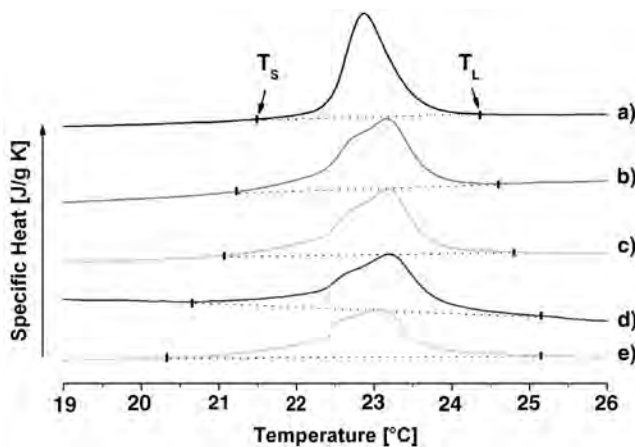

Figure 10 Thermograms. DSC thermogram of DMPC/DMPG without (a) myosin II and with myosin II ($b \rightarrow e$). Conditions: Lipid and myosin II concentration: 14.62 mM, and (b) 0.62 μM, (c) 1.45 μM, (d) 3.12 μM and (e) 6.24 μM, respectively.

3.1. Results

Myosin II insertion into phospholipid membranes was demonstrated using calorimetric measurements. The measurements were performed with multilamellar vesicles (MLVs) at 10 mg/ml consisting of DMPC/DMPG at a molar ratio of 50:50. Using increasing myosin concentrations, the changes in main phase transition were recorded ($P_{\beta'} \leftrightarrow L_\alpha$) as shown in Fig. 7. Adding increasing myosin II concentration (traces $b \rightarrow e$; $0.62 \rightarrow 6.24$ μM) to the lipid solution (a; no myosin II), a widening and flattening of the peak curvature was observed (Fig. 10). The start (T_S) and endpoint (T_L) of the phase transition are indicated by the arrows. The relative widening calculated from the relation, $(\Delta T_{1/2} - \Delta T^0_{1/2})/\Delta T^0_{1/2}$ is shown in Fig. 11. For a better comparison of the changes induced by the various myosin II concentrations, the enthalpy changes, ΔH, were normalized to pure lipids, against ΔH_0 (Table 1). Plotting the enthalpy changes $\Delta H/\Delta H_0$ against the molar ratios of myosin II and
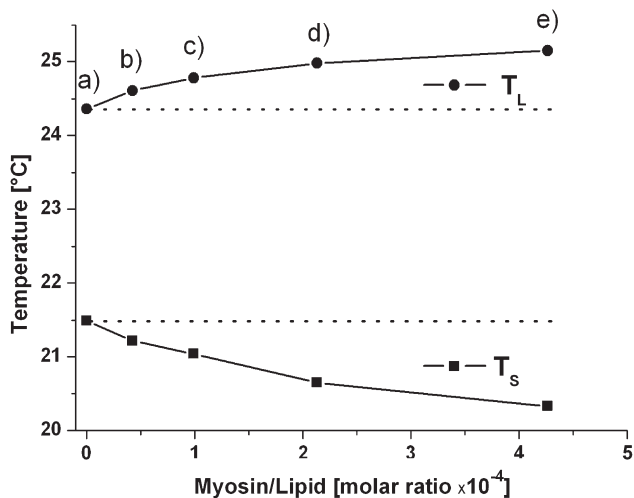
Figure 11 Phase transitions. A plot of T_S (solidus points) and T_L (liquidus points) taken from Fig. 10 as a function of myosin II–lipid molar ratio.

Table 1 Normalizing myosin II concentration against constant lipid concentration and enthalpy changes ΔH against ΔH_0 (lipids only).

Lipid	Myosin (µM)	Myosin/Lipid	$\Delta H/\Delta H_0$	Trace
$10\,mg/ml \cong 14.62\,mM$	0	0	1	a
	0.62	1/23580	0.91251	b
	1.45	1/10080	0.86383	c
	3.12	1/4690	0.74985	d
	6.24	1/2345	0.70055	e

lipids, an initial linear relationship followed by a saturation behavior of the lipid vesicles for myosin II was observed. The control protein BSA showed no changes (Fig. 12). Thermodynamic measurements (DSC) proved sufficient to determine the insertion behavior of myosin II into lipid membranes composed of DMPG/DMPC *in vitro* and the light scatter (stopped–flow) method confirmed these findings. The binding affinity of myosin II associated with and without lipids and actin was of a similar order of magnitude, confirming the previous observations of other membrane–interacting proteins [16].

4. SOLID-STATE NMR SPECTROSCOPY

Among the biophysical techniques that allow the investigation of peptides and proteins in bilayer environments solid-state NMR spectroscopy has proven to be a valuable tool. Recently, magic angle sample spinning solid-state NMR has resulted in the first NMR structures in the solid state of proteins in a microcrystalline
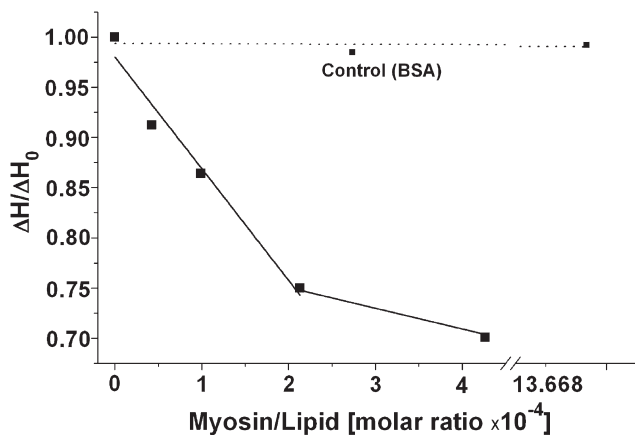
Figure 12 DSC plots. A plot of the changes in enthalpy $\Delta H / \Delta H_0$ against myosin II–lipid molar ratio. Bovine serum albumine (BSA) was used as a control protein.

environment [22] or when exhibiting a highly ordered microenvironment [23]. Furthermore, the technique makes accessible the structure, dynamics and topology of membrane-associated polypeptides (reviewed, e.g., in Refs. [24–27]). Using static-oriented samples, the tilt angles of helices with respect to the bilayer normal have been determined [28], and by measuring a large number of conformational constraints this approach has also been shown to be suitable for the complete structure determination of membrane-bound peptides [23,29]. In this chapter, we demonstrate how the orientation-dependence of NMR interactions is used to extract angular constraints from such static-oriented samples.

Proton-decoupled ^{15}N solid-state NMR spectroscopy of peptides labeled at the backbone amides with ^{15}N has been proven particularly convenient as this method provides the approximate tilt angle of membrane-associated helices in a direct manner [27,28]. Whereas transmembrane helical peptides exhibit ^{15}N chemical shifts around 200 ppm, sequences oriented parallel to the surface resonate at frequencies < 100 ppm (Figs. 13A and B).

In a similar manner the deuterium quadrupole splitting of the alanine $-C^2H_3$ groups is dependent on the alignment of the polypeptide relative to the membrane normal [30]. The technique has been used to study the membrane-channel domains of the viral proteins Vpu [31] and M2 [32,33] also in the presence of the channel blocker amantadine [34]. Furthermore antibiotic peptides have been studied in some detail using oriented solid-state NMR spectroscopy, including protegrin 1 [35], pardaxin [36], peptaibols [37–39], melittin [40] or magainins [41]. A family of designed histidine-containing antimicrobial peptides, which is also efficient during the transfection of nucleic acids into cells [42], exhibits transmembrane alignments at neutral pH but reorients to the membrane surface at acidic conditions [43]. By using solid-state NMR spectroscopy it was possible to show that the peptide exhibits its most pronounced antimicrobial properties when oriented parallel to the membrane surface [44] suggesting that the detergent-like properties of amphipathic peptides are essential for membrane permeation [45].
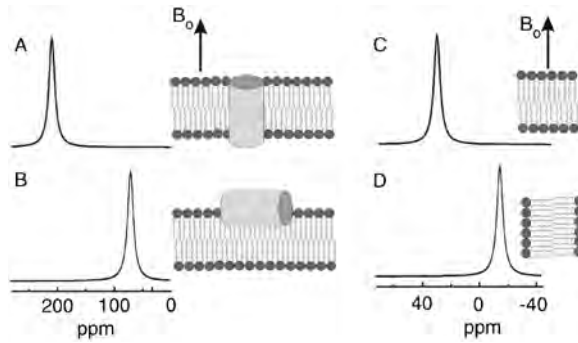
Figure 13 Simulated solid-state NMR spectra. (A) and (B) show simulated ^{15}N solid-state NMR spectra of an α-helical polypeptide oriented with the helix long axis perpendicular (A) or parallel (B) relative to the bilayer surface. The membranes are aligned with their normal parallel to the magnetic field of the NMR spectrometer (B_0). (C) and (D) show ^{31}P solid-state NMR spectra of liquid crystalline phosphatidylcholine membranes oriented with the lipid long axes parallel (C) or perpendicular (D) to B_0.

4.1. Theory: The Anisotropy of Interactions Measured in Solid-State NMR Spectroscopy

The nuclear interactions with the magnetic field are inherently anisotropic and, therefore, dependent on the orientation and conformation of the molecule with respect to the magnetic field direction [46–49]. Whereas in solution fast molecular tumbling ensures isotropic averaging of the nuclear interactions, the re-orientational correlation times of molecules that are associated with extended phospholipid bilayers are slow. Therefore, the anisotropic properties of these interactions are reflected in the NMR spectra of membrane-bound peptides or lipids.

The anisotropic chemical shift interaction is mathematically expressed by second rank tensors, which in the principal axis system is described by three orthogonal components σ_{11}, σ_{22} and σ_{33} (for a more detailed explanation see Ref. [28]). This tensor can be transformed into other coordinate systems by successive rotations. The component of the chemical shift tensor in direction of the magnetic field direction (z-direction) corresponds to the measured NMR chemical shift value. When expressed in terms of the Euler angles (Θ and Φ) and the principal elements of the chemical shift tensor σ_{11}, σ_{22} and σ_{33}, the measureable σ_{zz} amounts to

$$\sigma_{ZZ} = \sigma_{11}\sin^2\Theta\cos^2\Phi + \sigma_{22}\sin^2\Theta\sin^2\Phi + \sigma_{33}\cos^2\Theta \qquad (11)$$

Whereas the static ^{15}N chemical shift tensor of the amide bond exhibits σ_{22} and σ_{11} values in the 85 ppm and 65 ppm range, respectively, its σ_{33} component is characterized by a much different value of approximately 230 ppm [50–54]. In α-helical peptides the NH vector and the σ_{33} component cover an angle of about $18°$ and both are oriented within a few degrees of the helix long axis. Due to the unique size of σ_{33} and its orientation almost parallel to the helix axis it is possible to measure an approximate alignment of the helix within oriented phospholipid bilayers merely by recording the ^{15}N chemical shift interaction. Therefore, in

samples uniaxially oriented with the membrane normal parallel to the magnetic field transmembrane α-helical peptides exhibit ^{15}N resonances > 200 ppm (Fig. 13A). In contrast, they resonate in the $\sigma_{11}-\sigma_{22}$ range (i.e., < 100 ppm) when aligned parallel to the membrane surface (Fig. 13B). To arrive at a detailed structural analysis of solid–state NMR spectra from oriented samples, motional averaging and its effects on the chemical shift anisotropy have to be taken into consideration, however, the above analysis suffices for a semi-quantitative first analysis of polypeptide–membrane interactions.

Furthermore the deuterium spectra of methyl group labeled alanines in oriented membrane polypeptide sample have been analyzed. The methyl group of alanine exhibits fast rotational motions around the C_α–C_β bond. As a result the ^{2}H tensor is axially symmetric with respect to the C_α–C_β bond vector, and the measured splitting Δv_Q is directly related to the orientation of the $C_\alpha-C_\beta$ bond:

$$\Delta v_Q = \frac{3}{2}\frac{e^2 q Q}{h}\frac{(3\cos^2\Theta - 1)}{2} \tag{12}$$

where Θ is the angle between C_α–C_β bond and the magnetic field direction and $e^2 q Q/h$ the static quadrupolar coupling constant [55]. As C_α is an integral part of the polypeptide backbone, the orientation of the C_α–C_β bond also reflects the overall alignment of the peptide.

Due to fast axial rotation of the phospholipids around their long axis the ^{31}P chemical shift is characterized by an averaged symmetric tensor. The singular axis ($\sigma_{||}$) coincides with the rotational axis, i.e., the bilayer normal. In the ^{31}P solid–state NMR spectra of pure liquid crystalline phosphatidylcholine bilayers the signal at 30 ppm is thus indicative of phosphatidylcholine molecules with their long axis oriented parallel to the magnetic field direction (Fig. 13C), whereas a -15 ppm ^{31}P chemical shift is obtained for perpendicular alignments (Fig. 13D). In perfectly aligned samples the phospholipid bilayer spectra consists of a single line. Intensities to the right of this peak can arise from phospholipids with molecular orientations deviating from parallel to the magnetic field direction. In addition, signals in this region (< 30 ppm) can be due to local conformational changes of the phospholipid head group, for example due to electrostatic interactions of the ($-HPO_4^-$–CH_2–CH_2–$N^+(CH_3)_3$) dipoles of the phosphocholine head group, hydrogen bonding and/or electric dipole–dipole interactions [56,57]. We routinely record ^{31}P NMR spectra of phospholipid bilayers also of the peptide carrying samples to test for the quality of order and alignment of phospholipid bilayers.

4.2. Experimental Considerations

The peptides investigated by solid-state NMR investigations can be made available either by biochemical overexpression or by chemical solid-phase peptide synthesis. Whereas the former technique is well suited for uniform or selective labeling schemes, the chemical approach allows for specific labeling of one or a few amino acid residues. For example the talin peptide H17 with the sequence GEQIA̲Q-LIAGYIDIILKKKKSK-amide was prepared using automatic solid-phase peptide synthesis. At the underlined positions the ^{15}N-labeled analogue of alanine was

incorporated. The peptide synthetic products are commonly analyzed and purified using reversed phase high-performance liquid chromatography and their identity confirmed by mass spectrometry.

Typically, 10–15 mg of the polypeptide is reconstituted into about 100–200 mg of phospholipid by co-dissolving the compounds in organic solvents or organic solvent–water mixtures. For sample preparations encompassing the talin peptide hexafluoroisopropanol has proven a good choice. On the other hand, the denaturation of larger proteins should be avoided by the usage of aqueous buffers during the reconstitution process. Typically the mixtures are dried onto 30 ultra-thin cover glasses (9 × 22 mm), where applicable, the organic solvents completely removed and the samples equilibrated at 93% relative humidity. The glass plates are then stacked on top of each other, which results in small brick-shaped samples of 3–4 mm thickness (Fig. 14). These are stabilized and sealed with teflon tape and plastic wrappings. To ensure an optimal filling factor special NMR coils have been developed and tested for these samples [58]. These are flattened in such a manner to reduce the empty space within the coil (Fig. 14). Considerable improvements in signal–to–noise ratio can be achieved by this modification when compared to standard commercial solid-state NMR coils [58]. The membrane normal is aligned parallel to the magnetic field direction but alternative sample alignments have also been investigated, e.g., when the dynamic properties of the membrane-associated peptide are of interest [33,40,59]. Cross-polarization or Hahn echo NMR pulse

Figure 14   Solid-state NMR probe. The coils geometry has been adapted to the sample geometry. A stack of glass plates with several thousand lipid bilayers in between each pair is shown to the top left. The samples are protected and sealed before insertion into the flattened coil of the NMR probe. Before acquisition the NMR probe is introduced into the NMR magnet with the normal of the glass plates being oriented parallel to the magnetic field direction (Reproduced with permission).

sequences are typically used to acquire ^{15}N, ^{2}H and ^{31}P NMR spectra with the details given in previous publications, for example in Ref. [59,60].

4.3. Results and Discussion

Previous studies indicate the H17 exhibits membrane association predominantly driven by hydrophobic interactions and with partitioning constants in the $10^4\,M^{-1}$ range thereby being comparable to that of posttranslationally attached membrane anchors [61]. During the transfer from the aqueous to the membrane-associated state H17 undergoes a conformational transition from random coil to 86% α-helix [61]. The proton–decoupled ^{15}N solid-state NMR spectrum of the talin peptide H17 labeled with ^{15}N at the alanine-5 position exhibits a chemical shift of 80 ppm (Fig. 15). This value is indicative of an alignment of the peptide helix at the labeled site approximately parallel to the membrane surface [28]. The range of ^{15}N chemical shift values that is obtained from α-helices oriented at tilt angles of 60°, 70°, 80° or 90° (perfect in–plane alignment) are shown below the spectrum (Fig. 15A). This comparison indicates that the peak maximum of the ^{15}N maximum is in agreement with tilt angles of 70°–90°. This slightly oblique alignment is in excellent agreement
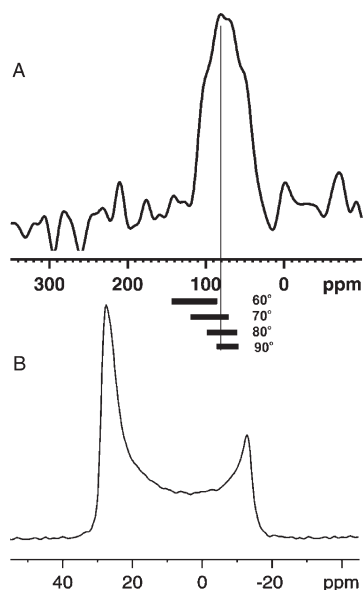

Figure 15 Solid-state NMR spectra of the talin peptide in oriented phospholipid membranes. (A) Proton-decoupled ^{15}N solid-state NMR spectra of 11 mg of the talin peptide reconstituted into 200 mg of 1-palmitoyl-2-oleoyl-*sn*-glycero-3-phosphocholine (POPC) membranes. The mixture has been applied onto glass surfaces, which are oriented with their normal parallel to the magnetic field direction. The bars indicate the calculated ^{15}N chemical shift range for peptides oriented at the indicated tilt angles relative to the membrane normal [27]. For the simulations the static main tensor elements were 223, 75 and 61 ppm with an alignment of the tensor elements as described in Ref. [54]. (B) Proton-decoupled ^{31}P solid-state NMR spectrum of the sample shown in panel A. The ^{31}P NMR line shape represents the distribution of alignments of the phospholipid head group in the sample.

with molecular modeling calculations, which predict a tilt angle of $72°$ [62] as well as with an area of insertion of $150\,\text{Å}^2$, i.e., about 50% of the projection of the helix onto the membrane surface [61].

However, the peak exhibits a considerable line width indicating that other conformations and/or peptide alignments are also present at the labeled site. The signal extends up to 110 ppm, a chemical shift value that is indicative of helix alignments in the $50°–75°$ range and/or reorientational averaging. At least two different explanations offer themselves to explain the heterogeneity observed at the labeled site. First, the alanine 5 position is relatively close to the N-terminus of the peptide leaving the possibility that the helical structure is not very stable and in conformational exchange. Second, it is possible that the helix as a whole adopts a variety of alignments by slowly wobbling back and forth.

The ^{31}P NMR spectrum of the same sample indicates that the peptide indeed exhibits a pronounced bilayer disordering effect (Fig. 15B). Although a main signal intensity is observed in the 30 ppm region considerable intensities extend throughout the chemical shift anisotropy of a liquid crystalline phosphatidylcholine bilayer. These additional ^{31}P signal intensities indicate that the lipid head group region exhibits a wide distribution of membrane alignments relative to the membrane normal. Interestingly, the H17 peptide from talin has been shown to exhibit fusogenic activities [62], a process that modifies the membrane curvature and requires a high degree of local rearrangements of the membrane.

Although more solid-state NMR experiments would be required to establish a detailed model of the structure and the dynamics of the talin peptide in phospholipid bilayers, the data already demonstrate the basic principles on how oriented solid-state NMR allows one to test not only the topology of membrane-associated peptides but also the polypeptides' influence on the lipid bilayer macroscopic phase properties.

To describe the tilt angle more accurately or to fully determine the structure of membrane-associated polypeptides by solid-state NMR spectroscopy additional angular constraints are accessible. These can be derived, for example, from the ^{15}N or ^{13}C chemical shift positions [40,63,64], ^{15}N–^{1}H dipolar coupling measurements [65–67] or ^{2}H quadrupolar interactions [30]. This latter approach has been particularly valuable as the deuterium NMR measurements provide additional information on the mosaicity of membrane alignment [68] as well as the rotational diffusion rate and thereby the aggregation state of the peptides [69].

It should be noted that the solid-state NMR data develop their full strength when it is possible to combine them with results from other investigations as has been shown for amphipathic peptide antibiotics, transfection peptides [42–44], a peptide from *ras* [70] or the H17 peptide described here [61,62].

5. Fluorescence Recovery after Photobleaching (FRAP)

Anchorage-dependent cells adhere to substrates through the ligation of transmembrane proteins, called integrins to extracellular matrix (ECM) molecules like

fibronectin, collagen and vitronectin [71]. The ligation and clustering of integrins gives rise to the recruitment of a variety of proteins like talin, vinculin and α-actinin [72] that physically connect integrins to the intracellular actin cytoskeleton (Fig. 16), resulting in the formation of a multi-protein complex called the 'focal adhesion' [72]. The focal adhesion forms a physical path for transferring intracellular forces generated in the contractile actin cytoskeleton which are transmitted through integrins onto the ECM substrate. Importantly, mechanical forces generated in the actin cytoskeleton promote adhesion assembly [73,74]. However, the underlying mechanisms are unclear.

Externally applied mechanical forces regulate the composition and the concentration of macromolecules that localize within focal adhesions. Focal adhesion assembly also regulates soluble signaling pathways, including Erk signaling that controls cell growth [75]. A variety of signal transduction pathways that control cell shape, gene expression, differentiation and apoptosis are triggered by integrin ligation [75–81]. Forces applied to beads that are ligated to integrin receptors induce a variety of responses including cAMP signaling [82–85], Ca^{2+} influx (through mechanosensitive ion channels), cytoskeletal remodeling [84], alterations of cell shape [85,86] and changes in nuclear morphology [87]. Thus, the focal adhesion is really a nano-scale mechano-chemical machine that transduces mechanical forces into intracellular biochemical signals, and therefore mediates both
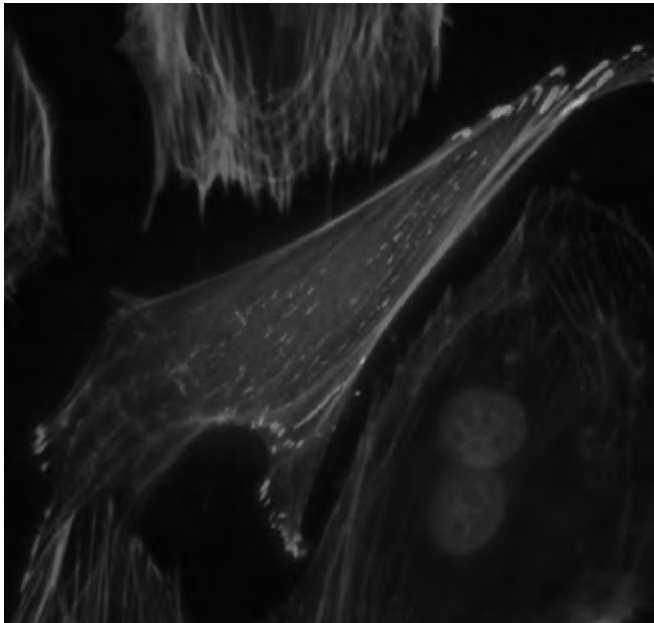

Figure 16 Fluorescence images. Fluorescence image of a single capillary endothelial cell expressing GFP-vinculin (green), stained for F-actin with Alexa phalloidin (red) and nuclei with DAPI (blue). Note: how each actin stress fiber is anchored into focal adhesions at its distal ends (bar = 10 μm). Reproduced with permission from Ref. [103], Copyright (c) 2006, Wiley-Liss, Inc. (please see plate no. 6 in the color section).

chemical and physical control of cellular physiology by ECM and mechanical forces.

5.1. Focal Adhesions and the Plasma Membrane

The formation of focal adhesions causes an increase in the levels of phosphatidylinositol-4,5-bisphosphate (PIP$_2$) [88,89], while antibodies to (PIP$_2$) inhibits adhesion assembly [90]. The adhesion protein vinculin interacts with (PIP$_2$) leading to vinculin activation, which promotes its binding to other adhesion proteins like talin and VASP [90]. Scaffold proteins localized to adhesions like α-actinin and filamin also bind to (PIP$_2$) [91–93]. Interactions between adhesion proteins and the lipid membranes may expose cryptic-binding sites leading to adhesion assembly, activate the *rho* pathway and promote actin filament assembly through membrane-tethered proteins like N-WASP [94]. The formation of focal adhesions may also regulate the formation of rafts at the lipid membrane; recent studies suggest that adhesion formation results in more order at the lipid membrane than caveolae [95]. Measuring the binding kinetics of proteins anchored to the living plasma membrane and other binding partners in focal adhesions may shed light on membrane-regulated mechanisms of adhesion assembly and regulation. In this chapter, we review our results on measuring the dissociation rate constants of vinculin, a membrane-associated adhesion protein, and zyxin, an adhesion protein that indirectly associates with the lipid membrane through binding interactions with α-actinin [9].

5.2. Quantifying Protein–Protein Binding Kinetics Inside Living Cells

Methods discussed previously in this chapter focused on measuring binding affinities between proteins *in vitro*. Complementary methods that can similarly quantify binding kinetics inside living cells are needed. This may help understand how protein–protein binding interactions may be regulated through intracellular signaling pathways, and how this may influence cellular physiology. For example, mechanical force may alter the binding kinetics of individual adhesion proteins through force-dependent modulation of protein conformation. This may result in net assembly of disassembly of molecules into adhesions. To test this hypothesis, methods that can quantify the binding kinetics of individual proteins inside a living cell are necessary. Such methods in combination with knowledge gained from *in vitro* studies of purified proteins may result in greatly increased insight of how multi-protein complexes are self-assembled, and how they function.

5.3. Method and Setup of FRAP

The diffusion coefficient of proteins inside living cells can be determined using laser photobleaching techniques, such as FRAP [96–98] in conjunction with mathematical models [99–102]. In FRAP, fluorescently labeled molecules within a small region of the surface membrane, cytoplasm or nucleus are exposed to a brief pulse of radiation from a laser beam at the excitation wavelength of the fluorophore (Fig. 17). This irradiation bleaches all the molecules within the path of the beam
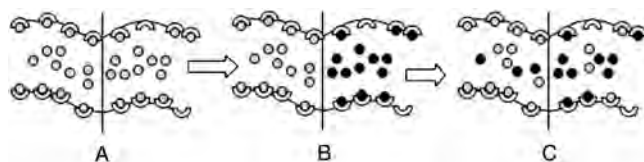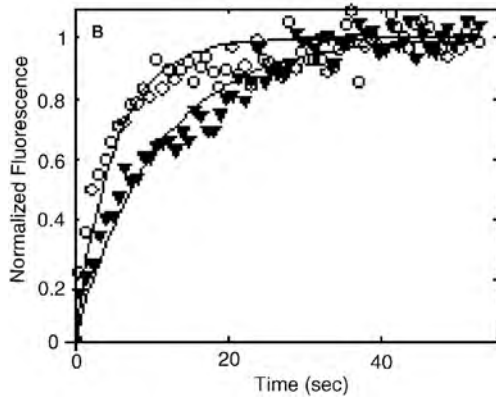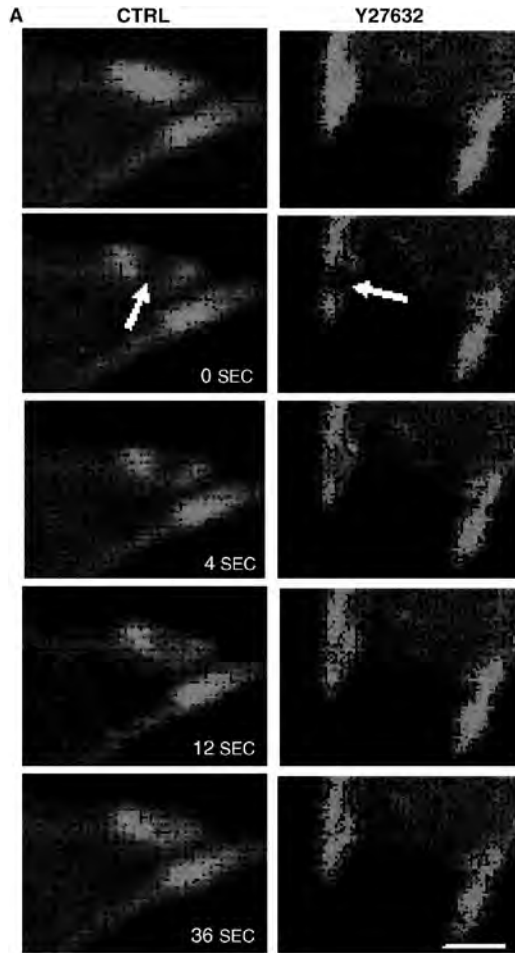
Figure 17 Diagram of molecular behavior during FRAP. (A) Before photobleaching, the bound molecules are in equilibrium with the free molecules. After photobleaching, there are two different modeling assumptions, (B) photobleached molecules are still bound to binding sites, and (C) exchange between fluorescent and bleached bound molecules, along with diffusive mixing leads to recovery (grey circles, fluorescent molecules; black circles, photobleached molecules). Reproduced from Ref. [104] with permission.

without altering their structure or function. Repeated fluorescence images of the bleached zone can be used to measure the rate at which fluorescent molecules redistribute and replace photo-bleached ones. If there is significant binding of molecules to structures in the bleached spot, fluorescence recovery will occur not only from diffusion, but rather from the interplay between binding–unbinding and diffusion. Thus, FRAP data can be potentially employed to make estimates of parameters that characterize the diffusion coefficient, binding rate constant and unbinding rate constant of proteins inside living cells [100]. This provides a significant advantage over biochemical methods that study molecules in solution because it permits analysis of the influence of cellular microenvironments on molecular interactions.

FRAP experiments are typically carried out using laser-scanning confocal microscopes like the Zeiss LSM 510 or the Leica TCS SP2 microscopes. In a laser-scanning confocal microscope, the fluorescence image is created by raster-scanning a highly focused excitation (laser) beam across the sample and recording the emitted fluorescence with a photomultiplier. The image is generated by combining individual pixel data into a computer-generated image. This mode of operation is particularly useful for FRAP experiments, because arbitrary shapes in the sample can be bleached during the raster scan by ramping up laser power selectively in pre-defined areas of the sample, while keeping the incident intensity at zero levels elsewhere. An acousto-optical tunable modulator (AOM) is used to increase the incident laser intensity in very short times (microseconds) in pre-defined bleached spots. Having bleached pre-defined areas, the subsequent recovery in fluorescence can be recorded by capturing fluorescence images over defined time intervals.

5.4. Results

FRAP experiments were performed on the Zeiss LSM 510 META/NLO microscope using a 63X 0.95 NA IR corrected water immersion lens. The 488 nm line of an Argon/2 multiple-lined single-photon laser source (10% of full power) was used for GFP excitation; 100% of the 488 nm line was used for photo-bleaching with 10 iterations corresponding to less than a millisecond. The size of the photo-bleached spot was chosen to be less than a square micron (Fig. 18A). Images were

collected using the Zeiss LSM 510 software (version 3.2). All experiments on microscopes were performed at 37°C using a temperature-controlled stage.

FRAP experiments revealed that zyxin, a focal adhesion protein and putative mechanosensor exchanges with the cytoplasm in several seconds (Fig. 18A). Cells were then treated with Y27632, a small molecule inhibitor that inhibits myosin II phosphorylation, and reduces mechanical force exerted by stress fibers on the focal adhesion. This accelerated the rate of fluorescence recovery of zyxin, while that of vinculin, another adhesion protein remains unchanged. This effect of mechanical force on the exchange rates of zyxin was captured in different types of experiments including laser-severing of individual stress fibers or changing ECM stiffness that ultimately altered the mechanical force exerted on adhesion sites.

5.5. Quantitative Analysis of FRAP Experiments

Fluorescence recovery occurs in the photo-bleached spot (Fig. 18B) because photo-bleached zyxin unbinds from the focal adhesion with a dissociation rate constant k_{OFF} and is replaced by a fluorescent molecule which rebinds with a rate constant k_{ON}. Fluorescent molecules in the cytoplasm diffuse with a diffusion coefficient D (Fig. 19). Cytoplasmic diffusion coefficients of proteins of the size of zyxin have a diffusion coefficient of a few microns/second. Based on cytoplasmic diffusion coefficients, the diffusion time for zyxin across the 60 nm thickness of the adhesion is on the order of a few milliseconds. Studies of focal adhesion ultrastructure suggest that the interstitial pore size is on the order of 10–30 nm [103]. Given that the size of proteins is on the order of 3–5 nm, the protein size is much smaller than the interstitial size inside focal adhesions. Hence, the interstitial diffusion coefficient of zyxin is not expected to be significantly different from that inside the cytoplasm. To explain the time scales observed for zyxin (Fig. 18A) purely based on diffusion, the interstitial diffusion coefficient would have to be 0.001 square micron/second, a number that is unreasonably low given the difference in protein size and adhesion pore size.

When diffusion is not rate limiting, the recovery of the fluorescence can be described by the differential equation $\mathrm{d}\hat{C}_F/\mathrm{d}t = k_{ON}SC_F - k_{OFF}\hat{C}_F$ and $\hat{C}_F(0) = \alpha\hat{C}_0$. Here, $\hat{C}_F$ is the concentration of bound fluorescent protein, C_F is the concentration of freely diffusing protein, S is the concentration of available binding sites, $\hat{C}_0 = k_{ON}SC_F/k_{OFF}$ is the pre-bleach concentration in the focal adhesion, and α denotes the fraction of fluorescent molecules that are not bleached in the photo-bleached spot. Making the assumption that C_F is constant (satisfied when

Figure 18 FRAP analysis of GFP zyxin recovery within individual photobleached focal adhesions. (A) Representative images of a FRAP experiment in control *versus* Y27632-treated cells showing that force dissipation accelerates zyxin recovery. Arrows indicate photobleached spots within individual focal adhesions that are analyzed over a period of 36 seconds follow photobleaching (bar = 2 μm). (B) Recovery curve for zyxin in control (open circles) *versus* Y27632-treated cells (closed triangles) from the experiment shown in A; solid lines are curves fit to the data using the method of least squares to estimate the dissociation rate constant k_{OFF} (please see plate no. 7 in the color section).
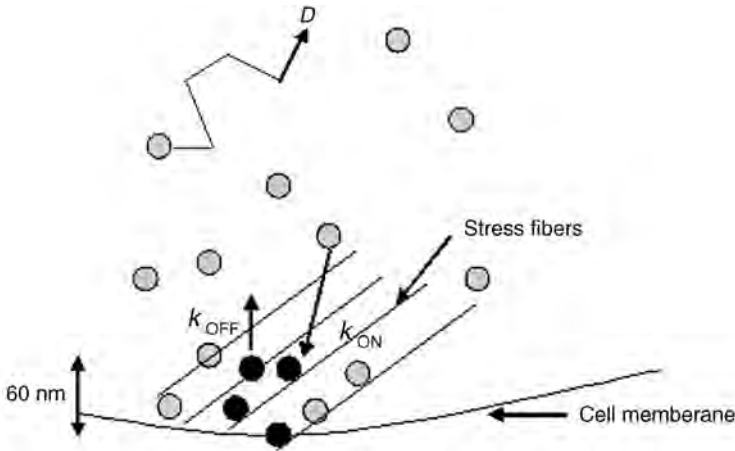
Figure 19 Schematic representation of FRAP. Schematic picture of molecular processes underlying exchange between the cytoplasmic diffusing protein and the adhesion-bound protein during FRAP. The black molecules indicate photobleached molecules, the rest are fluorescent. The vertical dimension of the adhesion is 60 nm, implying that the diffusive length scale is very small and arguing against diffusion being the rate limiting step (see text).

there is minimum photo-bleaching of cytoplasmic diffusing protein, and if the cytoplasmic diffusion is very fast compared to recovery times in the adhesion itself); the solution to the differential equation is $\hat{C}_F - \alpha\hat{C}_0/\hat{C}_0 - \alpha\hat{C}_0 = 1 - e^{-k_{OFF}t}$. Hence, normalized fluorescence recovery in the FRAP experiments yield k_{OFF} in Fig. 18B.

Decreasing the force exerted on the focal adhesions using Y27632 resulted in a continuous time-dependent increase in k_{OFF} of zyxin [103], with the average value of k_{OFF} increasing nearly 2.5-fold [103]. Laser ablation experiments in which individual stress fibers were cut to relax tension showed a similar increase in k_{OFF} in the anchored adhesion. Surprisingly, similar experiments with vinculin revealed that the values of k_{OFF} corresponding to both of its two dynamically distinct subpopulations remained unchanged after treatment with Y27632 [103]. Thus, the molecular-binding kinetics of some, but not all, focal adhesion proteins are selectively sensitive to changes in cytoskeletal tension.

The k_{OFF} measured in these experiments is really an 'effective' rate constant. This is because a protein may bind to multiple binding partners inside cells simultaneously. Further experiments that measure similar properties *in vitro* for protein–protein pairs may be useful in interpreting the intracellular data. FRAP experiments combined with systematic molecular biology experiments (relying on mutagenesis, deletion, etc.) that interfere with specific interactions in cells may also be useful to tease out pair-wise contributions to the time scales. In conclusion, a judicious combination of the *in vitro* methods and *in vivo* methods discussed in this chapter may help yield unprecedented insight into the molecular mechanisms of protein function at the cytoskeletal-lipid interface.

ACKNOWLEDGEMENTS

REFERENCES

[1] G. Isenberg, Actin binding proteins – lipid interactions, J. Muscle Res. Cell Motil. 12 (1991) 136–144; (review).

[2] E.J. Luna, A.L. Hitt, Cytoskeleton–plasma membrane interactions, Science 258 (1992) 955–964; (review).

[3] G. Isenberg, W.H. Goldmann, Actin binding proteins–lipid interactions, in: J.E. Hesketh, I.F. Pryme (Eds.), The Cytoskeleton, Vol. 1, Jai Press Inc., Greenwich, NY, 1995, pp. 169–204.

[4] G. Isenberg, New concepts for signaling perception and transduction by the actin cytoskeleton at cell boundaries, Semin. Cell Dev. Biol. 7 (1996) 707–715.

[5] G. Isenberg, V. Niggli, Interaction of cytoskeletal proteins with membrane lipids, Int. Rev. Cytol. 178 (1998) 73–125. (review).

[6] V. Niggli, Structural properties of lipid-binding sites in cytoskeletal proteins, Trends Biochem. Sci. 26 (2001) 604–611; (review).

[7] J. Smith, G. Diez, A.H. Klemm, V. Schewkunow, W.H. Goldmann, CapZ–lipid membrane interactions: a computer analysis, Theor. Biol. Med. Model. 3 (2006) 30.

[8] W.H. Goldmann, J.M. Teodoridis, C.P. Sharma, B. Hu, G. Isenberg, Fragments from actin binding protein (ABP-280; filamin) insert into reconstituted lipid layers, Biochem. Biophys. Res. Commun. 259 (1999) 108–112.

[9] W.H. Goldmann, J.M. Teodoridis, C.P. Sharma, J.L. Alonso, G. Isenberg, Fragments from alpha-actinin insert into reconstituted lipid bilayers, Biochem. Biophys. Res. Commun. 264 (1999) 225–229.

[10] W.H. Goldmann, J.L. Niles, M.A. Arnaout, Interaction of purified human proteinase 3 (PR3) with reconstituted lipid bilayers, Eur. J. Biochem. 261 (1999) 155–162.

[11] D.L. Scott, G. Diez, W.H. Goldmann, Protein–lipid interactions: correlation of a predictive algorithm for lipid-binding sites with three-dimensional structural data, Theor. Biol. Med. Model. 3 (2006) 17; (review).

[12] H. Gutfreund, Enzymes: Physical Principles, John Wiley & Sons, London, 1972, pp. 1–242.

[13] C.F. Bernasconi, Relaxation Kinetics, Academic Press, New York, 1976, pp. 34–39.

[14] W.H. Goldmann, Z. Guttenberg, R.M. Ezzell, G. Isenberg, The study of fast reactions by the stopped-flow method, in: G. Isenberg, (Ed.), Modern Optics, Electronics, and High Precision Techniques in Cell Biology, Springer–Verlag, Heidelberg, 1998, pp. 159–171.

[15] W.H. Goldmann, M.A. Geeves, A 'slow' temperature jump apparatus build from a stopped-flow machine, Anal. Biochem. 192 (1991) 55–58.

[16] W.H. Goldmann, R. Senger, S. Kaufmann, G. Isenberg, Determination of the affinity of talin and vinculin to charged lipid vesicles: a light scatter study, FEBS Lett. 368 (1995) 516–518.

[17] N. Michel, A.S. Fabiano, A. Polidori, R. Jack, B. Pucci, Determination of phase transition temperatures of lipids by light scattering, Chem. Phys. Lipids 139 (2006) 11–19.

[18] K. Hiromi, Kinetics of Fast Reactions – Theory and Practice, Halsted Press, New York, 1979, pp. 99–104.

[19] J.M. Sturtevant, Biochemical applications of differential scanning calorimetry, Annu. Rev. Phys. Chem. 38 (1987) 463–488.

[20] A. Watts, Protein–lipid interactions, in: A. Neuberger, L.L.M. van Deenen (Eds.), New Comprehensive Biochemistry, Vol. 25, Elsevier, Amsterdam, 1993, pp. 1–379.

[21] I. Jelesarov, H.R. Bosshard, Isothermal titration calorimetry and differential scanning calorimetry as complementary tools to investigate the energetics of biomolecular recognitions, J. Mol. Recognit. 12 (1999) 3–18.

[22] F. Castellani, B. van Rossum, A. Diehl, M. Schubert, K. Rehbein, H. Oschkinat, Structure of a protein determined by solid-state magic-angle-spinning NMR spectroscopy, Nature 420 (2002) 98–102.

[23] A. Lange, K. Giller, S. Hornig, M.F. Martin-Eauclaire, O. Pongs, S. Becker, M. Baldus, Toxin-induced conformational changes in a potassium channel revealed by solid-state NMR, Nature 440 (2006) 959–962.

[24] J.H. Davis, M. Auger, Static and magic angle spinning NMR of membrane peptides and proteins, Prog. NMR Spectrosc 35 (1999) 1–84.

[25] A. Watts, Direct studies of ligand–receptor interactions and ion channel blocking (review), Mol. Membr. Biol. 19 (2002) 267–275.

[26] A. Drechsler, F. Separovic, Solid-state NMR structure determination, IUBMB Life 55 (2003) 515–523.

[27] B. Bechinger, C. Aisenbrey, P. Bertani, Topology, structure and dynamics of membrane-associated peptides by solid-state NMR spectroscopy, Biochim. Biophys. Acta 1666 (2004) 190–204.

[28] B. Bechinger, C. Sizun, Alignment and structural analysis of membrane polypeptides by 15N and 31P solid-state NMR spectroscopy, Concepts Magn. Reson. 18A (2003) 130–145.

[29] T.A. Cross, Solid-state nuclear magnetic resonance characterization of gramicidin channel structure, Meth. Enzymol. 289 (1997) 672–696.

[30] C. Aisenbrey, B. Bechinger, Tilt and rotational pitch angles of membrane-inserted polypeptides from combined 15N and 2H solid-state NMR spectroscopy, Biochemistry 43 (2004) 10502–10512.

[31] B. Bechinger, P. Henklein, Solid-state NMR investigations of Vpu structural domains in oriented phospholipid bilayers: interactions and alignment, in: W. Fischer (Ed.), Viral Membrane Proteins: Structure, Function, Drug Design, Vol. 1, in: M. Zouhair Atassa (Ed.), Series Protein Reviews, Springer-Verlag, Heidelberg, 2005, pp. 177–186, Chapter 13.

[32] Z.Y. Song, F.A. Kovacs, J. Wang, J.K. Denny, S.C. Shekar, J.R. Quine, T.A. Cross, Trans-membrane domain of M2 protein from influenza A virus studied by solid-state N-15 polarization inversion spin exchange at magic angle NMR, Biophys. J. 79 (2000) 767–775.

[33] C. Aisenbrey, P. Bertani, P. Henklein, B. Bechinger, Structure, dynamics and topology of membrane polypeptides by oriented ^{2}H solid-state NMR spectroscopy, Eur. Biophys. J. 36 (2007) 451–460.

[34] B. Bechinger, R. Kinder, M. Helmle, T.B. Vogt, U. Harzer, S. Schinzel, Peptide structural analysis by solid-state NMR spectroscopy, Biopolymers 51 (1999) 174–190.

[35] J.J. Buffy, A.J. Waring, R.I. Lehrer, M. Hong, Immobilization and aggregation of the antimicrobial peptide protegrin-1 in lipid bilayers investigated by solid-state NMR, Biochemistry 42 (2003) 13725–13734.

[36] K.J. Hallock, D.K. Lee, J. Omnaas, H.I. Mosberg, A. Ramamoorthy, Membrane composition determines pardaxin's mechanism of lipid bilayer disruption, Biophys. J. 83 (2002) 1004–1013.

[37] C.L. North, M. Barranger-Mathys, D.S. Cafiso, Membrane orientation of the N-terminal segment of alamethicin determined by solid-state ^{15}N NMR, Biophys. J. 69 (1995) 2392–2397.

[38] B. Bechinger, D.A. Skladnev, A. Ogrel, X. Li, N.Y. Swischewa, T.V. Ovchinnikova, J.D.J. O'Neil, J. Raap, ^{15}N and ^{31}P solid-state NMR investigations on the orientation of zervamicin II and alamethicin in phosphatidylcholine membranes, Biochemistry 40 (2001) 9428–9437.

[39] M. Bak, R.P. Bywater, M. Hohwy, J.K. Thomsen, K. Adelhorst, H.J. Jakobsen, O.W. Sorensen, N.C. Nielsen, Conformation of alamethicin in oriented phospholipid bilayers determined by N-15 solid-state nuclear magnetic resonance, Biophys. J. 81 (2001) 1684–1698.

[40] R. Smith, F. Separovic, T.J. Milne, A. Whittaker, F.M. Bennett, B.A. Cornell, A. Makriyannis, Structure and orientation of the pore-forming peptide, melittin, in lipid bilayers, J. Mol. Biol. 241 (1994) 456–466.

[41] B. Bechinger, The structure, dynamics and orientation of antimicrobial peptides in membranes by solid-state NMR spectroscopy, Biochim. Biophys. Acta 1462 (1999) 157–183.

[42] A. Kichler, C. Leborgne, J. März, O. Danos, B. Bechinger, Histidine-rich amphipathic peptide antibiotics promote efficient delivery of DNA into mammalian cells, Proc. Natl. Acad. Sci. U.S.A. 100 (2003) 1564–1568.

[43] B. Bechinger, Towards membrane protein design: pH dependent topology of histidine-containing polypeptides, J. Mol. Biol. 263 (1996) 768–775.

[44] T.C.B. Vogt, B. Bechinger, The interactions of histidine-containing amphipathic helical peptide antibiotics with lipid bilayers: the effects of charges and pH, J. Biol. Chem. 274 (1999) 29115–29121.

[45] B. Bechinger, K. Lohner, Detergent-like action of linear cationic membrane-active antibiotic peptides, Biochim. Biophys. Acta. 1758 (2006) 1529–1539.

[46] U. Haeberlen, High Resolution NMR in Solids, Selective Averaging, Academic Press, New York, 1976.

[47] M. Mehring, Principles of High Resolution NMR in Solids, Springer-Verlag, Berlin, 1983.

[48] T.A. Cross, J.R. Quine, Protein structure in anisotropic environments: development of orientational constraints, Concepts Magn. Reson. 12 (2000) 55–70.

[49] R.G. Griffin, Solid-state nuclear magnetic resonance of lipid bilayers, Meth. Enzymol. 72 (1981) 108–173.

[50] C.J. Hartzell, M. Whitfield, T.G. Oas, G.P. Drobny, Determination of the ^{15}N and ^{13}C chemical shift tensors of L- [^{13}C]alanyl-L-[^{15}N]alanine from the dipole-coupled powder patterns, J. Am. Chem. Soc. 109 (1987) 5966–5969.

[51] D.K. Lee, R.J. Wittebort, A. Ramamoorthy, Characterization of ^{15}N chemical shift and 1H-15N dipolar coupling interactions in a peptide bond of uniaxially oriented and polycrystalline samples by one-dimensional dipolar chemical shift solid-state NMR spectroscopy, J. Am. Chem. Soc. 120 (1998) 8868–8874.

[52] D.K. Lee, Y. Wei, A. Ramamoorthy, A two-dimensional magic-angle decoupling and magic-angle turning solid-state NMR method: an application to study chemical shift tensors from peptides that are nonselectively labeled with ^{15}N isotope, J. Phys. Chem. B 105 (2001) 4752–4762.

[53] T.G. Oas, C.J. Hartzell, F.W. Dahlquist, G.P. Drobny, The amide 15N chemical shift tensors of four peptides determined from 13C dipole-coupled chemical shift powder patterns, J. Am. Chem. Soc. 109 (1987) 5962–5966.

[54] N.D. Lazo, W. Hu, T.A. Cross, Low-temperature solid-state ^{15}N NMR characterization of polypeptide backbone librations, J. Magn. Reson. 107 (1995) 43–50.

[55] J. Seelig, Deuterium magnetic resonance: theory and application to lipid membranes, Q. Rev. Biophys. 10 (1977) 353–418.

[56] P.G. Scherer, J. Seelig, Electric charge effects on phospholipid headgroups. Phosphatidycholine in mixtures with cationic and anionic amphiles, Biochemistry 28 (1989) 7720–7727.

[57] B. Bechinger, J. Seelig, Interaction of electric dipoles with phospholipid head groups. A ^2H and ^{31}P NMR study of phloretin and phloretin analogues in phosphatidylcholine membranes, Biochemistry 30 (1991) 3923–3929.

[58] B. Bechinger, S.J. Opella, Flat-coil probe for NMR spectrscopy of oriented membrane samples, J. Magn. Reson. 95 (1991) 585–588.

[59] C.B.B. Aisenbrey, B. Bechinger, Investigations of polypeptide rotational diffusion in aligned membranes by ^2H and ^{15}N solid-state NMR spectroscopy, J. Am. Chem. Soc. 126 (2004) 16676–16683.

[60] B. Bechinger, Detergent-like properties of magainin antibiotic peptides: a 31P solid-state NMR study, Biochim. Biophys. Acta 1712 (2005) 101–108.

[61] A. Seelig, X.L. Blatter, A. Frentzel, G. Isenberg, Phospholipid binding of synthetic talin peptides provides evidence for an intrinsic membrane anchor of talin, J. Biol. Chem. 275 (2000) 17954–17961.

[62] G. Isenberg, S. Doerhoefer, D. Hoekstra, W.H. Goldmann, Membrane fusion induced by the major lipid-binding domain of the cytoskeletal protein talin, Biochem. Biophys. Res. Commun. 295 (2002) 636–643.

[63] T.A. Cross, Solid-state nuclear magnetic resonance characterization of gramicidin channel structure, Meth. Enzymol. 289 (1997) 672–696.

[64] V. Wray, R. Kinder, T. Federau, P. Henklein, B. Bechinger, U. Schubert, Solution structure and orientation of the transmembrane anchor domain of the HIV-1 encoded virus protein U (Vpu) by high-resolution and solid-state NMR spectroscopy, Biochemistry 38 (1999) 5272–5282.

[65] B. Bechinger, M. Zasloff, S.J. Opella, Structure and interactions of magainin antibiotic peptides in lipid bilayers: a solid-state NMR investigation, Biophys. J. 62 (1992) 12–14.

[66] A. Ramamoorthy, C.H. Wu, S.J. Opella, Experimental aspects of multidimensional solid-state NMR correlation spectroscopy, J. Magn. Reson. 140 (1999) 131–140.

[67] S.J. Opella, F.M. Marassi, J.J. Gesell, A.P. Valente, Y. Kim, M. Oblatt-Montal, M. Montal, Structures of the M2 channel-lining segments from nicotinic acetylcholine and NMDA receptors by NMR spectroscopy, Nat. Struct. Biol. 6 (1999) 374–379.

[68] C. Aisenbrey, C. Sizun, J. Koch, M. Herget, R. Abele, B. Bechinger, R. Tampe, Structure and dynamics of membrane-associated ICP47, a viral inhibitor of the MHC I antigen-processing machinery, J. Biol. Chem. 281 (2006) 30365–30372.

[69] C. Aisenbrey, B. Bechinger, Investigations of peptide rotational diffusion in aligned membranes by ^{2}H and ^{15}N solid-state NMR spectroscopy, J. Am. Chem. Soc. 126 (2004) 16676–16683.

[70] D. Huster, A. Vogel, C. Katzka, H.A. Scheidt, H. Binder, S. Dante, T. Gutberlet, O. Zschornig, H. Waldmann, K. Arnold, Membrane insertion of a lipidated ras peptide studied by FTIR, solid-state NMR, and neutron diffraction spectroscopy, J. Am. Chem. Soc. 125 (2003) 4070–4079.

[71] R.O. Hynes, Integrins: bidirectional, allosteric signaling machines, Cell 110 (2002) 673–687.

[72] A.D. Bershadsky, N.Q. Balaban, B. Geiger, Adhesion-dependent cell mechanosensitivity, Annu. Rev. Cell Dev. Biol. 19 (2003) 677–695.

[73] N.Q. Balaban, U.S. Schwarz, D. Riveline, P. Goichberg, G. Tzur, I. Sabanay, D. Mahalu, S. Safran, A.D. Bershadsky, L. Addadi, B. Geiger, Force and focal adhesion assembly: a close relationship studied using elastic micropatterned substrates, Nat. Cell Biol. 3 (2001) 466–472.

[74] D. Riveline, E. Zamir, N.Q. Balaban, U.S. Schwarz, T. Ishizaki, S. Narumiya, Z. Kam, B. Geiger, A.D. Bershadsky, Focal contacts as mechanosensors: externally applied local mechanical force induces growth of focal contacts by an mDia1-dependent and ROCK-independent mechanism, J. Cell Biol. 153 (2001) 1175–1186.

[75] Q. Chen, M.S. Kinch, T.H. Lin, K. Burridge, R.L. Juliano, Integrin-mediated cell adhesion activates mitogen-activated protein kinases, J. Biol. Chem. 269 (1994) 26602–26605.

[76] K. Burridge, K. Wennerberg, Rho and Rac take center stage, Cell 116 (2004) 167–179.

[77] A.J. Ridley, M.A. Schwartz, K. Burridge, R.A. Firtel, M.H. Ginsberg, G. Borisy, J.T. Parsons, A.R. Horwitz, Cell migration: integrating signals from front to back, Science 302 (2003) 1704–1709.

[78] K.A. DeMali, K. Wennerberg, K. Burridge, Integrin signaling to the actin cytoskeleton, Curr. Opin. Cell Biol. 15 (2003) 572–582.

[79] S.K. Sastry, K. Burridge, Focal adhesions: a nexus for intracellular signaling and cytoskeletal dynamics, Exp. Cell Res. 261 (2000) 25–36.

[80] K. Burridge, M. Chrzanowska-Wodnicka, Focal adhesions, contractility, and signaling, Annu. Rev. Cell Dev. Biol. 12 (1996) 463–518.

[81] L.H. Romer, K. Burridge, C.E. Turner, Signaling between the extracellular matrix and the cytoskeleton: tyrosine phosphorylation and focal adhesion assembly, Cold Spring Harb. Symp. Quant. Biol. 57 (1992) 193–202.

[82] D.R. Overby, F.J. Alenghat, M. Montoya-Zavala, H.C. Bei, P. Oh, J. Karavitis, D.E. Ingber, Magnetic cellular switches, IEEE Trans. Magn. 40 (2004) 2958–2960.

[83] B.D. Matthews, D.R. Overby, R. Mannix, D.E. Ingber, Cellular adaptation to mechanical stress: role of integrins, Rho, cytoskeletal tension, and mechanosensitive ion channels, J. Cell Sci. 119 (2006) 508–518.

[84] D.R. Overby, B.D. Matthews, E. Alsberg, D.E. Ingber, Novel dynamic rheological behavior of focal adhesions measured within single cells using electromagnetic pulling cytometry, Acta Biomater. 3 (2005) 295–303.

[85] C.S. Chen, J.L. Alonso, E. Ostuni, G.M. Whitesides, D.E. Ingber, Cell shape provides global control of focal adhesion assembly, Biochem. Biophys. Res. Commun. 307 (2003) 355–361.

[86] A. Brock, E. Chang, C.C. Ho, P. LeDuc, X. Jiang, G.M. Whitesides, D.E. Ingber, Geometric determinants of directional cell motility revealed using microcontact printing, Langmuir 19 (2003) 1611–1617.

[87] A.J. Maniotis, C.S. Chen, D.E. Ingber, Demonstration of mechanical connections between integrins, cytoskeletal filaments, and nucleoplasm that stabilize nuclear structure, Proc. Natl. Acad. Sci. U.S.A. 94 (1997) 849–854.

[88] H.P. McNamee, H.G. Liley, D.E. Ingber, Integrin-dependent control of inositol lipid synthesis in vascular endothelial cells and smooth muscle cells, Exp. Cell Res. 224 (1996) 116–122.

[89] H.P. McNamee, D.E. Ingber, M.A. Schwartz, Adhesion to fibronectin stimulates inositol lipid synthesis and enhances PDGF-induced inositol lipid breakdown, J. Cell Biol. 121 (1993) 673–678.

[90] A.P. Gilmore, K. Burridge, Regulation of vinculin binding to talin and actin by phosphatidyl-inositol-4-5-bisphosphate, Nature 381 (1996) 531–535.

[91] K. Fukami, N. Sawada, T. Endo, T. Takenawa, Identification of a phosphatidylinositol 4,5-bisphosphate-binding site in chicken skeletal muscle alpha-actinin, J. Biol. Chem. 271 (1996) 2646–2650.

[92] K. Fukami, K. Furuhashi, M. Inagaki, T. Endo, S. Hatano, T. Takenawa, Requirement of phosphatidylinositol 4,5-bisphosphate for alpha-actinin function, Nature 359 (1992) 150–152.

[93] K. Furuhashi, M. Inagaki, S. Hatano, K. Fukami, T. Takenawa, Inositol phospholipid-induced suppression of F-actin-gelating activity of smooth muscle filamin, Biochem. Biophys. Res. Commun. 184 (1992) 1261–1265.

[94] A.S. Sechi, J. Wehland, The actin cytoskeleton and plasma membrane connection: PtdIns(4,5)P(2) influences cytoskeletal protein activity at the plasma membrane, J. Cell Sci. 113 (2000) 3685–3695.

[95] K. Gaus, S. Le Lay, N. Balasubramanian, M.A. Schwartz, Integrin-mediated adhesion regulates membrane order, J. Cell Biol. 174 (2006) 725–734.

[96] E.D. Salmon, R.J. Leslie, W.M. Saxton, M.L. Karow, J.R. McIntosh, Spindle microtubule dynamics in sea urchin embryos: analysis using a fluorescein-labeled tubulin and measurements of fluorescence redistribution after laser photobleaching, J. Cell Biol. 99 (1984) 2165–2174.

[97] M. Schindler, M.J. Osborn, D.E. Koppel, Lateral diffusion of lipopolysaccharide in the outer membrane of Salmonella typhimurium, Nature 285 (1980) 261–263.

[98] K. Jacobson, Z. Derzko, E.S. Wu, Y. Hou, G. Poste, Measurement of the lateral mobility of cell surface components in single, living cells by fluorescence recovery after photobleaching, J. Supramol. Struct. 5 (1976) 565–576.

[99] D. Axelrod, D. Koppel, J. Schlessinger, E. Elson, W. Webb, Mobility measurement by analysis of fluorescence photobleaching recovery kinetics, Biophys. J. 16 (1976) 1055–1069.

[100] R. Phair, T. Misteli, Kinetic modelling approaches to in vivo imaging, Nat. Rev. Mol. Cell Biol. 2 (2001) 898–907.

[101] Y. Tardy, J. McGrath, J. Hartwig, C. Dewey, Interpreting photoactivated fluorescence micros-copy measurements of steady-state actin dynamics, Biophys. J. 69 (1995) 1674–1682.

[102] C.M. Franz, D.J. Muller, Analyzing focal adhesion structure by atomic force microscopy, J. Cell Sci. 118 (2005) 5315–5323.

[103] T.P. Lele, J. Pendse, S. Kumar, M. Salanga, J. Karavitis, D.E. Ingber, Mechanical forces alter zyxin unbinding kinetics within focal adhesions of living cells, J. Cell. Physiol. 207 (2006) 187–194.

[104] T.P. Lele, P. Oh, J.A. Nickerson, D.E. Ingber, An improved mathematical model for determination of molecular kinetics in living cells with FRAP, Mech. Chem. Biosys. 1 (2004) 181–190.